The Opposite Effect of Water and *N*-Methyl-2-Pyrrolidone Cosolvents on the Nanostructural Organization of Ethylammonium Butanoate Ionic Liquid: A Small- and Wide-Angle X-Ray Scattering and Molecular Dynamics Simulations Study

Umme Salma,[†] Natalia V. Plechkova,[§] Ruggero Caminiti,[†,‡] and Lorenzo Gontrani*[,†] [iD]

[†]Dipartimento di Chimica and [‡]Centro di Ricerca per le Nanotecnologie Applicate all' Ingegneria — CNIS, Università di Roma, "La Sapienza", Piazzale le Aldo Moro 5, I-00185 Roma, Italy

[§]The QUILL Research Centre, School of Chemistry and Chemical Engineering, the Queen's University of Belfast, Stranmillis Road, Belfast BT9 5AG, United Kingdom

S *Supporting Information*

ABSTRACT: Two series of mixtures of ethylammoniumbutanoate (EAB, $[N_{0\,0\,0\,2}][C_3CO_2]$) in water and N-methyl-2-pyrrolidone (NMP) have been prepared at different molar fractions to assess the effect of these two polar solvents on the nanostructural order present in $[N_{0\,0\,0\,2}][C_3CO_2]$. The small- and wide-angle X-ray scattering (SWAXS) pattern of the liquid in neat state shows a prepeak at $Q = 0.513$ Å^{-1}, which is associated with the aggregation of nonpolar alkyl chains of both cations and anions. Interestingly, the two solvents affect the nanostructure of $[N_{0\,0\,0\,2}][C_3CO_2]$ differently, though both are polar. In the case of water addition to the mixture, the prepeak shifts to lower Q values, while in NMP, it moves toward higher values. Also, the principal peaks move in opposite direction in both solvents. The underlying expansion (water) or contraction (NMP) of the solutions observed by the scattering experiments is discussed in terms of molecular dynamics (MD) simulations, which are in very good agreement with the observed patterns.
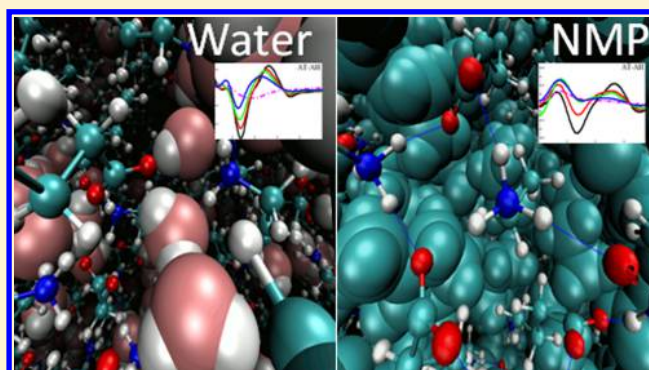
INTRODUCTION

Ionic liquids (ILs) are usually defined as salts whose melting points are below 100 °C;[1] if they melt below 25 °C they are referred as "room temperature" (RTILs).[2] The reason for the low melting points is the "packing frustration", which can be justified principally in terms of the low symmetry and charge delocalization of their molecular structures,[3] but some other factors such as conformational flexibility can come into play. These systems are commonly subdivided into aprotic ionic liquids (AILs) and protic ionic liquids (PILs);[4,5] the latter are prepared through the stoichiometric neutralization reaction of Brønsted acids and Brønsted bases. A fundamental property of PILs is that they have an acidic proton on the cation; the most known and studied example of such liquids is ethylammonium nitrate,[6] which shares the cationic part with the system of the present study.

Although various ILs have been synthesized and characterized so far, there is still a need for rationalization of their structural features. A variety of techniques, including diffraction, spectroscopic, and computational methods, have been employed to investigate interionic interactions, dynamics, and solvation phenomena in ILs.[7−9]

Aggregation in ILs is a phenomenon by which either or both the cations and anions interact with each other in solution to form local, highly charged phases.[10] In these cases, the aggregation results in the mesoscopic order of the system, which can be pointed out in small-angle X-ray scattering (SAXS) patterns in the form of prepeaks.[11] The scattering intensity of the prepeak is high when either cations or anions bear long alkyl chains, and becomes stronger when the alkyl chains are present on both ions.[12] Aggregation or self-assembly in various PILs was pinpointed from small- and wide-angle X-ray scattering (SWAXS) patterns of a wide range of alkylammonium, dialkylammonium, trialkylammonium, and cyclic ammonium cations combined with organic or inorganic anions.[13] The SWAXS peak positions and intensities were systematically characterized, confirming that nanostructure gets more pronounced with increasing cation amphiphilicity. The anion choice was also found to influence the degree of nanostructure, although the structural reason for this order could not be determined.[14]

Molecular dynamics (MD) simulations are a powerful tool to access condensed phase structure, but most of the simulation studies for ILs carried out so far concentrated on the local environment around a given cation or anion, providing results that agree with many of the features recognized in diffraction patterns. On the basis of computer simulations, the long-range structure of ionic liquids was discussed by Urahata and Ribeiro[15] using a united-atom model of imidazolium ILs. MD simulations are not only able to predict physical properties directly from a molecular interaction model, but also to access the structure at a molecular level. Harsha et al. reported the effect of water on the dynamics of 1-hexyl-3-methylimidazolium hexafluorophosphate using molecular dynamic simulations.[16]

The effect of water on the nanostructural organization of ILs has been a key focus due to its possible spillover in synthetic chemistry and catalysis.[17] It is, however, important to study the structure of ILs mixtures with other solvents as well to expand the applicability of ILs to industrial and technological applications. The study of aqueous mixtures is particularly important, since water is a universal solvent, an omnipresent compound, and is the most common contaminant in ILs due to their intrinsic hygroscopic nature. ILs drastically change physicochemical properties upon water addition;[18,19] G. Driver[20] states that "water molecules possess a higher degree of effective ionicity in the liquid salt environment relative to that of pure water (i.e., H_2O molecules can be highly ionised in ILs)". The selection of water as solvent with ethylammonium-butanoate (EAB) has already been reported.[21] In our previous reports,[22] we presented some SAXS experimental results on alkylammonium alkanoate ILs and the effect of water on their structure.

■ EXPERIMENT

Sample Synthesis. Ethylammonium butanoate was synthesized with the method used in our previously reported work.[23,24] Butanoic acid (1 mol, purchased from Sigma Aldrich; ≥ 99%) was added dropwise to an aqueous solution of ethylamine (1 mol, Sigma Aldrich; ≥ 99.5%) in a one-neck 250 cm^3-bottomed flask, cooled with liquid dinitrogen. The flask was kept closed after acid addition and cooled by adding more liquid dinitrogen, when necessary. The reaction is fairly exothermic, and maintaining the temperature low is important. The reaction was then left to warm up to room temperature for ca. 2 h and then stirred at room temperature for 1 h. The water was removed by freeze-drying, at 0.03 mbar pressure for three cycles. After a 12 h cycle, the water content was checked by Karl Fischer titration. The result showed a water mole fraction > 0.1 (Table 1), so the freeze-drying cycle was repeated twice more, until no decrease in the water content was observed. The resulting ethylammonium butanoate, Figure 1 (98% yield) is an extremely hygroscopic light yellow liquid, and therefore it was kept in the glovebox until use. After removing from the glovebox, $[N_{0\,0\,0\,2}][C_3CO_2]$ + water and $[N_{0\,0\,0\,2}][C_3CO_2]$ + NMP mixtures were prepared by weight in septum-capped vials of about 2 cm^3 using needles and syringes to transfer liquids. Before weighting, NMP was degassed for about 2 h by means of an ultrasonic device (WVR model USC100T −45 kHz, 30 W), while pure water was used immediately after distillation. The densities of the liquid mixtures and the pure compounds were measured at 298.15 K by means of a vibrating tube densitometer (model DMA 58, Anton Paar, Gratz, Austria).

X-ray Scattering. For both SAXS and wide-angle X-ray scattering (WAXS) experiments, about 0.3 mL of liquid were

Table 1. Water Mole Fraction (χ_{water}), Molar Ratio between EAB and Water (R) of Each Mixture, Experimental Density, Number of Water (N_{water}) and EAB Molecules (N_{EAB}) Used for Each Simulation Box Based on Concentration Ratio R, and Density from Molecular Dynamics Simulation

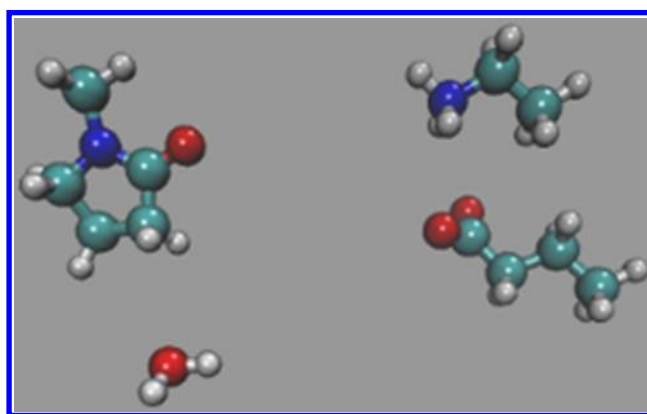| sample	χ_{water}	R (n_{water}/ n_{EAB})	experimental density (g/cm^3)	N_{EAB}	N_{water}	calculated density (g/cm^3)
χ_0	0.00	0.00	0.9620	550	0	0.9675
χ_1	0.39	0.41	0.9706	525	175	0.9992
χ_2	0.50	1.01	0.9801	500	500	1.0163
χ_3	0.70	2.02	0.9911	450	900	1.0292
χ_4	0.80	4.05	1.0035	375	1500	1.0455
χ_5	0.91	10.18	1.0136	250	2500	1.0585

Figure 1. Molecular structures of the cation (top right), anion (bottom right), NMP (top left) and water (bottom left).

introduced in an amorphous quartz capillary (2 mm diameter), that was afterward sealed with a Teflon band and kept in dry atmosphere, just before the measurements.

Small angle diffraction experiments (SAXS) were collected on a Bruker AXS D8 Advance focusing powder diffractometer operating in transmission mode in θ/θ geometry, equipped with a Cu-Kα X-Ray tube (λ = 1.5407 Å). Capillaries were fixed, upside down, using bee-wax, to a standard goniometer head and aligned along the beam path. The instrument is fitted with focusing Göbel mirrors along the incident beam, Soller slits on both incident (2.3° horizontal divergence) and diffracted (radial) beams, and a Vantec-1 position sensitive detector (PSD). Data were measured in step-scan mode in the 2−40° 2θ angular range, step-size 0.022° 2θ and 1s counting time. WAXS studies were instead carried out on a Bruker D8 Advance with DaVinci design diffractometer (angle dispersive) equipped with a Mo K$_\alpha$X-Ray tube (λ = 0.7107 Å) and with Göbel mirrors as in SAXS. The 2θ angle range available is 5−143° with a step of 0.103° within the Bragg−Brentano para-focusing geometry. The scattered intensity was gathered with the Lynxeye XE Energy-Dispersive 1-D detector.

After the corrections for the background and sample absorption and the subtraction of the independent atomic scattering that does not depend on the structure from raw data (I_{exp}), the "total (static) structure function" $I(Q)$ is obtained: Equation 1:

$$I(Q) = I_{EXP}(Q) - \sum_{i=1}^{N} x_i f_i(Q)^2 \tag{1}$$

The structure function is the structurally sensitive part of the scattering intensity, and originates from the interference contributions from different atoms; the variable Q is the magnitude of the transferred momentum, and depends on the scattering angle (2θ), according to the relation $Q = 4\pi (\sin \theta/\lambda)$.

The function $I(Q)$ is related to the partial radial distribution functions descriptive of the structure and obtainable from the simulations, according to eq 2:

$$I(Q) = \sum_{i=1}^{N} \sum_{i=1}^{N} x_i x_j f_i f_j 4\pi \rho_0 \int_0^{\infty} r^2 (g_{ij}(r) - 1) \frac{\sin(Qr)}{Qr} \, dr \tag{2}$$

In eqs 1 and 2, x_i and x_j are the numerical concentrations of the species, while f_i and f_j are their Q-dependent X-ray scattering factors, and ρ_0 is the bulk number density. Equation 2 is the link between experimental and model data, as the $g(r)$s can be calculated from molecular simulations.

Both the experimental and the theoretical structure functions were multiplied by a sharpening function $M(Q)$, necessary to improve the curve resolution at high Q, and then Fourier-transformed in the distance domain, according to eq 3:

$$\text{Diff}(r) = \frac{2r}{\pi} \int_0^{\infty} QI(Q)M(Q)r \sin (Q) \, dQ \tag{3}$$

In the differential correlation form (eq 3), only the structural contributions to the radial distribution are present, while the "uniform" contribution is left out. Comprehensive derivation of all the equations is described elsewhere.[25,26]

Summarizing, the analysis of both reciprocal space ($QI(Q)M(Q)$) and distance space ($\text{Diff}(r)$) functions is used to compare X-ray experimental data and simulations. This methodology has been successfully applied to the study[27,28] of molecular and ionic liquids,[29,30] as well as solutions.[31,32] For the comparative studies of the mixtures at low Q, the normalized structure function $S(Q)$ functions will also be used (see below).

Molecular Dynamics Simulations. Simulations were performed describing the potential energy with the two-body Generalized Amber Force Field (GAFF)[33] using the Amber/PMEMD v.12 package[34] as the molecular dynamics engine. The electrostatic interactions were modeled using the partial atomic charges obtained from restrained electrostatic potential (RESP) fitting[35] of the electrostatic potential for isolated cations and anions at the equilibrium geometry calculated at the B3LYP/6-31G* level. The initial configurations were generated randomly with the software Packmol[36] using a minimum interatomic separation of 2 Å as a constraint. The cubic boxes used had all an initial edge of 50 Å and were filled with the necessary numbers of ions/water molecules, based on the value of experimental density. The length of the edge was chosen as twice the average largest correlation distance of these systems, which was identified in the last detectable peak in experimental $\text{Diff}(r)$ distributions falling at about 25 Å.

The simulation protocol can be summarized as follows:

- Energy minimizations performed using both steepest descent and conjugated gradient methods.
- A short NVT run (20 ps) at 50 K
- Gradual heating at 298 K in the NPT ensemble using Berendsen weak coupling algorithm,[37] with external pressure set at 1 atm, followed by 2 ns NPT equilibration

at 298K. Coupling constants of 1 ps were used for both pressure and temperature.
- NPT 298K equilibration of about 2 ns.
- Productive NVT simulation for 2 ns with integration time step of 2 fs and trajectories collected every 1000 steps.

The trajectories were processed with in-house codes (X-ray patterns) and with g_rdf (Gromacs suite).[38]

■ RESULTS AND DISCUSSION

Within all the Q range scanned during the scattering measurements ($0-17$ Å^{-1}), in the lowest part ($0.2-2.5$ Å^{-1}), which is mainly related to intermolecular interactions, two evident features come out. The first peak ("pre-peak", or polarity−polarity peak according to Araque et al.[39]) appears at $Q = 0.513$ Å^{-1} in pure $[\text{N}_{0\,0\,0\,2}][\text{C}_3\text{CO}_2]$ spectra. Such peak, according to the literature, can be ascribed to the segregation of the apolar four-carbon alkyl chains of the anion from the charged polar heads. The following "principal" or "adjacency" peak is originated from the whole assortment of intermolecular and longer intramolecular distances, and depends on the average value of such contacts.

The most interesting phenomenon observed in the present study is the shift of both peaks when water or NMP is added: in the first case, the prepeak moves toward lower Q values, and principal peaks reach larger Q values, while the opposite behavior is observed in NMP. The details of peak positions of $[\text{N}_{0\,0\,0\,2}][\text{C}_3\text{CO}_2]$ + water (left) and $[\text{N}_{0\,0\,0\,2}][\text{C}_3\text{CO}_2]$ + NMP (right) mixtures are given in Table 3 and are plotted in Figure 3

Table 2. NMP Mole Fraction (χ_{NMP}), Molar Ratio (R) between EAB and NMP of Each Mixture, Experimental Density, Number of EAB (N_{EAB}) and NMP (N_{NMP}) Molecules Used for Each Simulation Box Based on Concentration Ratio R, Density from Molecular Dynamics Simulations

sample	χ_{NMP}	R ($n_{\text{NMP}}/n_{\text{EAB}}$)	experimental density (g/cm^3)	N_{EAB}	N_{NMP}	calculated density (g/cm^3)
χ_0	0.00	0.00	0.9620	550	0	0.9675
χ_1	0.31	0.40	0.9785	270	108	0.9992
χ_2	0.51	1.03	0.9924	180	180	1.0095
χ_3	0.67	2.06	1.0037	120	240	1.0185
χ_4	0.80	3.99	1.0123	100	400	1.0239
χ_5	0.91	10.14	1.0204	50	500	1.0311

Table 3. Peak Positions versus Composition of EAB+water Mixtures and EAB+NMP Mixtures[a]

	EAB+water mixtures			EAB+NMP mixtures	
sample	prepeak (Å^{-1})	principal peak (Å^{-1})	sample	prepeak (Å^{-1})	principal peak (Å^{-1})
χ_0	0.5137	1.4800	χ_0	0.5137	1.4800
χ_1	0.5000	1.4870	χ_1	0.5300	1.4500
χ_2	0.4800	1.4960	χ_2	0.5500	1.4100
χ_3	0.4500	1.5100	χ_3	0.5700	1.3600
χ_4	0.4090	1.5800	χ_4	-	1.3300
χ_5	0.3300	1.6900	χ_5	-	1.2900

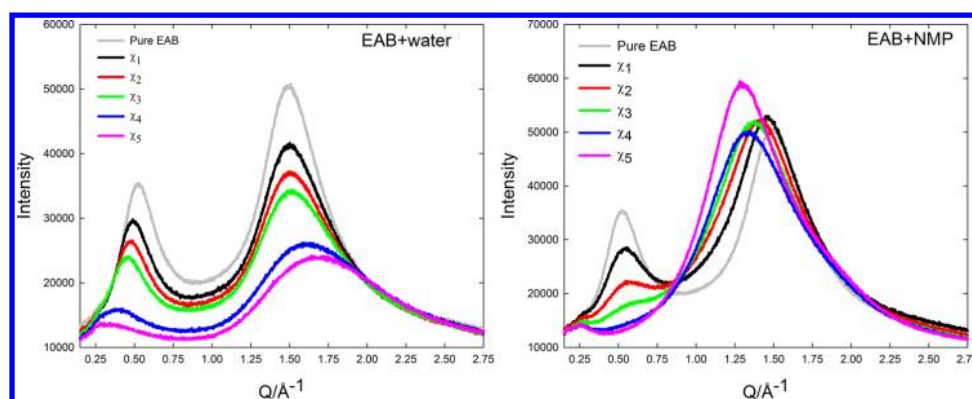[a]$\chi_0-\chi_5$ are the mole fractions of co-solvents (water and NMP) in EAB.

Figure 2. Experimental X-ray intensity patterns at small-medium Q of EAB−water (left) and EAB-NMP (right) mixtures. Color codes: gray pure EAB (χ_0), black χ_1, red χ_2, green χ_3, blue χ_4, magenta χ_5.
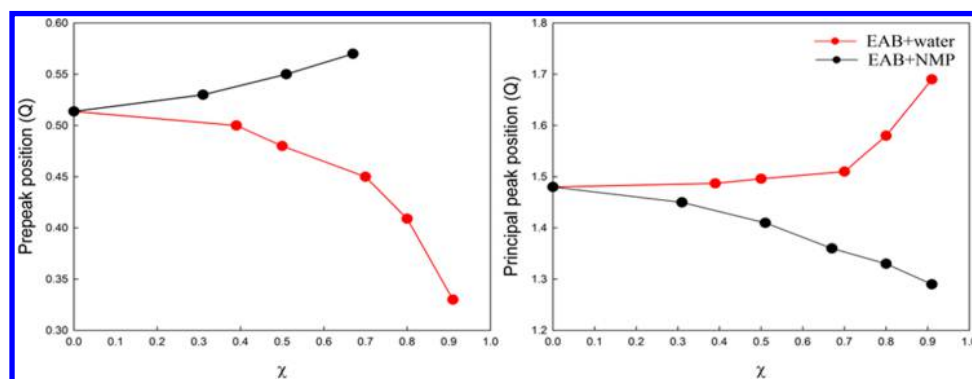

Figure 3. Positions of prepeak (left) and principal peaks of EAB in water and NMP as a function of cosolvent concentration.

as a function of $[\mathrm{N}_{0\,0\,0\,2}][\mathrm{C}_3\mathrm{CO}_2]$ concentration. By looking in detail, the first peak moves from 0.513 Å⁻¹ to 0.330 Å⁻¹ at the maximum water concentration where the peak is observable, corresponding to effective Bragg distances ($d = 2\pi/Q$) of 12.25 and 19.03 Å, respectively. The opposite trend is observed on the principal peak that passes from 1.48 to 1.69 Å⁻¹ with dilution. The prepeak shifts and its lowering can be interpreted in terms of the strong hydrogen bond interactions between water molecules and the polar ends of cation and anion, which have two effects: (1) the segregated alkyl chains are teased apart, water enters the structure acting as a spacer between the ions, and the system is gradually enlarged (larger mean distance = smaller Q) and (2) the relative weight of the structural correlation (as the number of particles interacting at the average reciprocal Bragg distance with respect to all the particles) decreases. The principal peak, vice versa, moves at larger Q values owing to the gradual replacement of $[\mathrm{N}_{0\,0\,0\,2}][\mathrm{C}_3\mathrm{CO}_2]$ with water molecules, that are significantly shorter (higher Q) than any of the two ions.

In EAB/NMP mixtures, conversely, the prepeak is shifted from 0.514 to 0.570 Å⁻¹ (12.22 and 11.02 Å) and the principal peak falls below 1.3 at the maximum NMP concentration. This trend could be interpreted in terms of the large steric hindrance of NMP ring plus methyl moieties, which would bring cations and anions closer. A pictorial representation of these phenomena is given in Figure 6, which shows two frames extracted from the trajectory obtained from EAB−H₂O and EAB−NMP simulations (intermediate composition χ_3). A confirmation of this interpretation can be found in the radial distribution functions between cation and anion centers of mass calculated in the simulations. It can be seen, in fact, that the
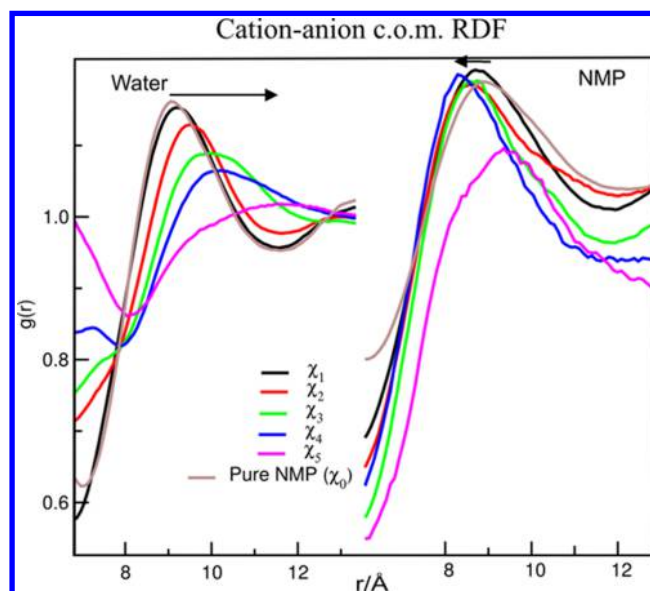

Figure 4. Radial Distribution functions between centers of mass. EAB-Water: left; EAB-NMP: right. Color codes: gray pure EAB (χ_0), black χ_1, red χ_2, green χ_3, blue χ_4, magenta χ_5.

position of the second-neighbor shell for these functions follows the same trend observed experimentally (Figure 4). Such effect is very evident for water and less pronounced (though visible) for NMP simulations. In this case, only the sample richest in cosolvent (χ_5) seems not to follow the calculated trend (Table 2). At that concentration, though, the
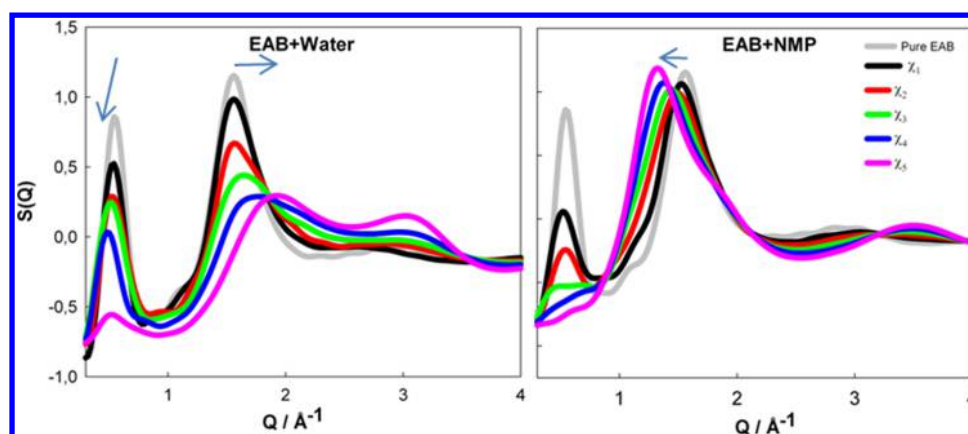
Figure 5. Theoretical normalized structure functions $S(Q)$ calculated theoretically for pure EAB and its mixtures with water (left panel) and NMP (right panel). Color codes: gray - pure EAB (χ_0), black χ_1, red χ_2, green χ_3, blue χ_4, magenta χ_5. The arrows are only a guide for the eye
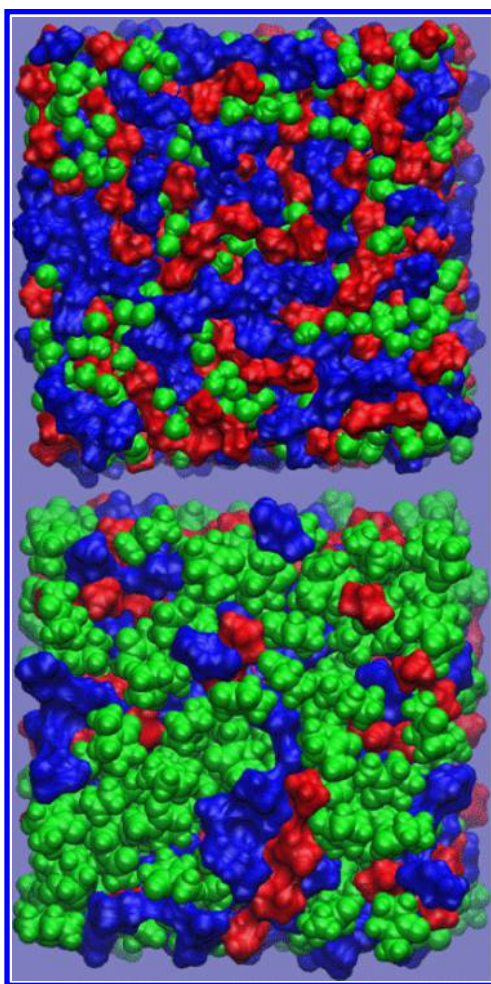

Figure 6. Snapshots from χ_3 samples simulations. Top: water, mixture. Bottom: NMP mixture. Cation: red, anion: blue, solvent: green.

IL is extremely diluted, and the excluded volume of NMP dominates; moreover, no prepeak is visible starting from χ_4.

◼ NORMALIZED AND TOTAL STRUCTURE FUNCTIONS

When systems of different composition are considered, the best way of comparing simulated X-ray patterns is through the normalized structure function: $\left(S(Q) = \frac{I(Q)}{\sum_{i=1}^{N} x_i f_i(Q)}\right)$, since in this formulation the intensity is normalized by the number concentrations x_i and the scattering power of the species f_i;[39−41] otherwise, the use of $I(Q)$ (eq 2) would give very different intensities for systems differing by the total number of electrons. The $S(Q)$ functions calculated from MD trajectories are reported in Figure 5 for both systems, and show that the experimental data of Figure 2 can be reproduced well, apart from the relative heights of the peaks as just mentioned. In particular, it can be seen how the prepeak gradually disappears with increasing water or NMP concentration, and how the principal peaks move toward those of pure water at 1.9 (going rightward) or NMP (going leftward). Moreover, in the water mixtures, the typical double-peak feature of liquid water (~1.9 and ~ 2.9 Å^{-1}) gradually builds up, as expected.

One of the most interesting aspects of using a theoretical model rests in the analysis of the contributions of the various ion fragments to the $S(Q)$s. This kind of partitioning approach has been successfully reported in several recent studies, e.g., by Kashyap et al.[42] or Dhungana et al.[43] and, in this case, further confirms the different behavior of the two cosolvents. For EAB system ions, four different moieties were considered: two head groups (carboxylate $COO^−$ anion head (AH) and ammonium NH_3^+ cation head (CH)) and two tail groups, consisting of the remaining alkyl groups of each ion (AT and CT). These partial $S(Q)$s were obtained by activating only the number concentrations of the corresponding atoms in eq 2, and by zeroing the other ones, followed by proper subtraction of the homologous terms if needed.

The results are reported in Figure 7 for water and in Figure 8 for NMP mixtures; cosolvent concentrations increase passing from black to magenta plots.

In the left columns, the correlation between the charged parts is reported. The top plot shows the AH−CH correlation in the range $2 < Q < 3.2$ Å^{-1} that roughly corresponds to the non bonding interactions ($d \approx 2\pi/Q = 2$−3.15 Å), like hydrogen-bonds, including the hydrogen-heavy atom distances.

The analysis indicates that the intensity of the correlation is rapidly damped in both cases, and for water it moves at lower Q; the peak shift is more evident for the like-charge correlations occurring in the range $0.8 < Q < 2$ Å^{-1} (longer distances), that are shown in the second and third left-column panels, and is clearer for CH−CH than AH−AH. Almost no shift is visible in
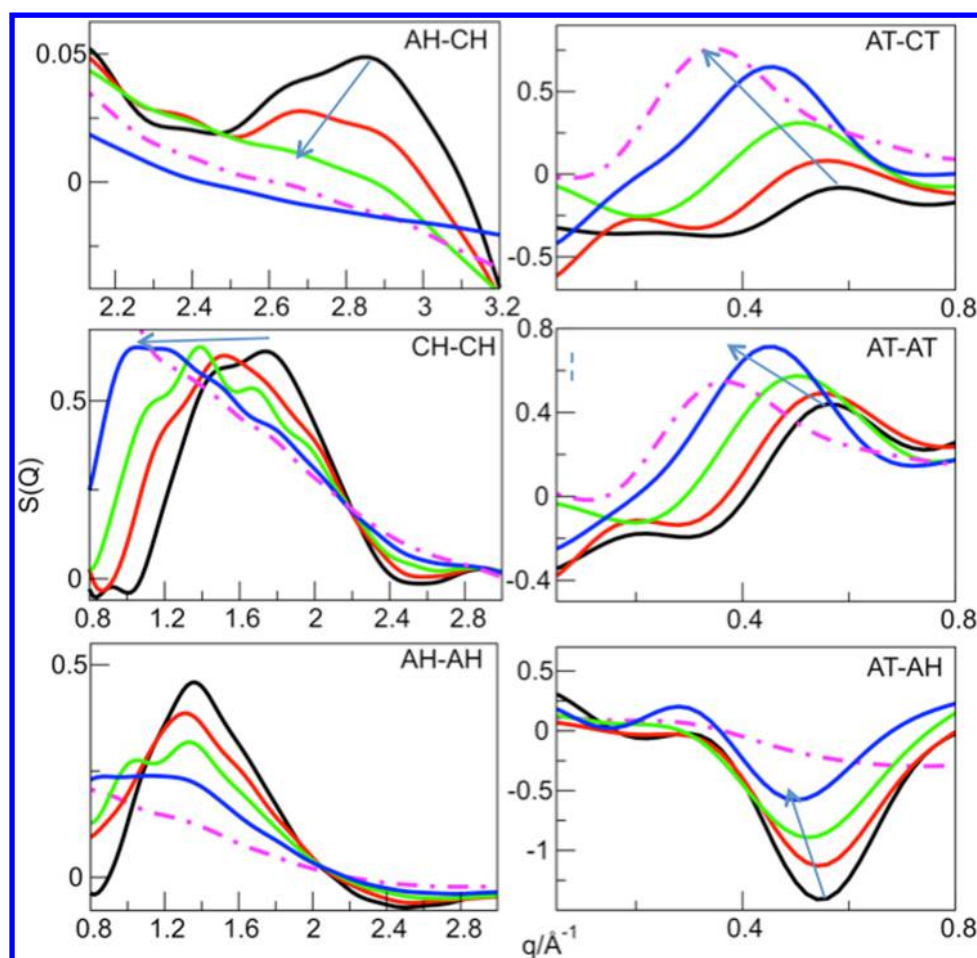
Figure 7. Partial normalized structure function $S(Q)$ for water−EAB mixtures. A = anion, C = cation, H = head, T = tail. Heads correspond to the NH_3 and COO fragments in cations and anions, respectively; tails are defined as the remaining atoms. Color codes: black χ_1, red χ_2, green χ_3, blue χ_4, magenta χ_5. The arrows are only a guide for the eye.

the analogous NMP plots. By comparing CH−CH and AH−AH for water, it appears that the intensity is less affected for cations, while in anion heads it shows marked reduction, hinting that anions interact with water more than cations. This finding is confirmed by the analysis of the water versus ions radial distribution function of the intermediate χ_3 mixture reported in Figure 9, left panel.

The $g(r)$ pattern regards the hydrogen bond contact (heavy atoms) between cation ammonium nitrogen and water oxygen and carboxylate oxygen−water oxygen for cation and anion, respectively. The plot shows that the interaction with anion heads occurs at shorter distance than cation heads, and that its occurrence is larger, as signaled by the integral of the peaks shown in the inset (the integral for the anion should be multiplied by two, the number of anion oxygen atoms). The two values are 2.64 and 2.07 at the peak right border, respectively.

The right columns of Figures 7 and 8 focus on the longer-range correlations in the range $0.2 < Q < 0.8$ Å^{-1} ($d \approx 7.8-31$ Å), corresponding to the experimental prepeak, and include the correlations where at least one partner is the anion tail. Also this range confirms, for water mixtures, the shift at lower Q of the positions of peaks and antipeaks. All these findings both point to an intercalating role of water that interacts with the ion heads, so that the less interacting and distant portions (tails) move apart. A representation of water insertion into IL

structure, and of water-ion interactions is given in Figure S4 of the Supporting Information.

Further insight can be obtained considering the water−water $S(Q)$ values, which are shown in Figure 9, right panel. This correlation suggests that water gets "structured" in the mixture following the ionic liquid correlations. The structure function for pure water (calculated, TIP4P model), which shows no features in that range, is reported for comparison.

In NMP solutions, the effect is almost absent; only a small shift toward higher Q is visible in the AT−AT and AH−AT correlations.

The comparison between experimental and model patterns on the whole Q range, particularly at high Q, is more easily feasible using the $QI(Q)M(Q)$ functions; they have the differential distribution function Diff(r) (eq 3) as the counterpart in the direct space. Both patterns are shown in Figure S1 (water) and Figure S2 (NMP) of the Supporting Information, and confirm the good quality of the simulation models in describing the systems. The only slight flaw of the models is the disagreement between theoretical and experimental densities, the former ones being 1−3% larger. The decrease of signal-to-noise ratio at high water content is worthy of note as well. This fact is due to the longer measuring times that would be needed to obtain smooth patterns for water, a small molecule with large mobility.
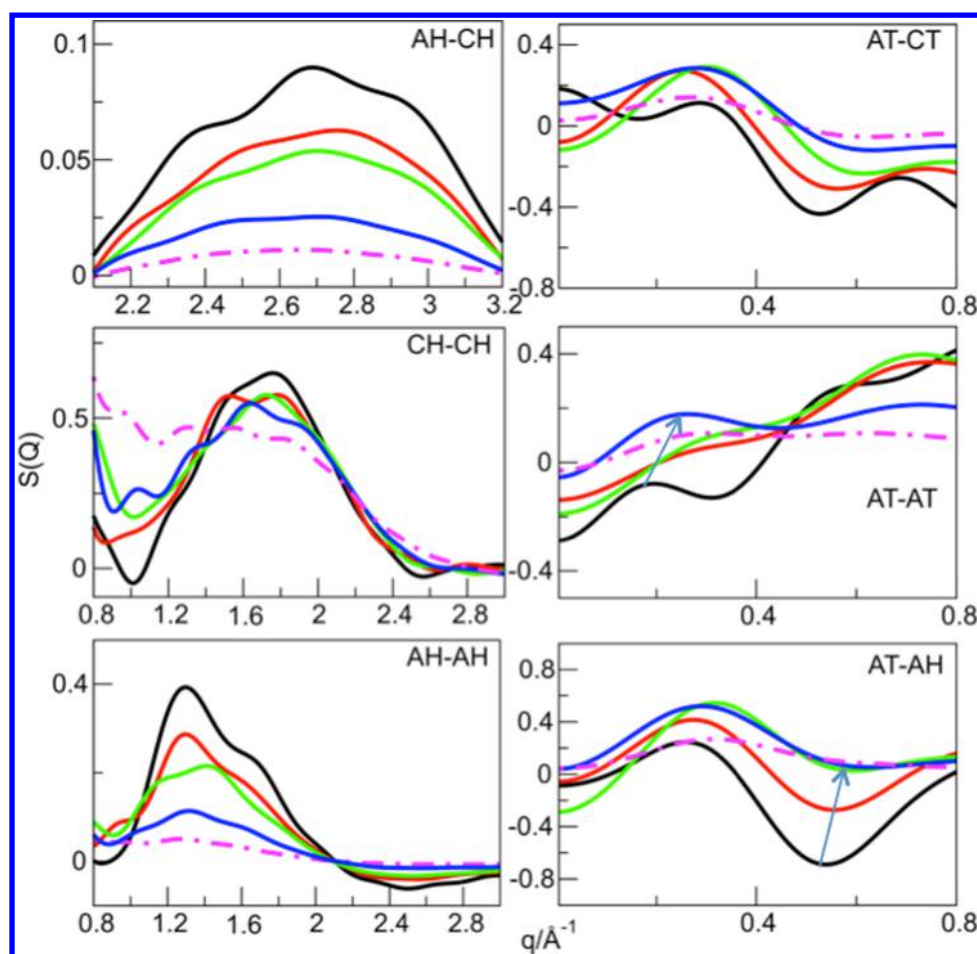
Figure 8. Partial normalized structure function $S(Q)$ for NMP−EAB mixtures. A = anion, C = cation, H = head, T = tail. Heads correspond to the NH_3 and COO fragments in cations and anions, respectively; tails are defined as the remaining atoms. Color codes: black χ_1, red χ_2, green χ_3, blue χ_4, magenta χ_5. The arrows are only a guide for the eye.
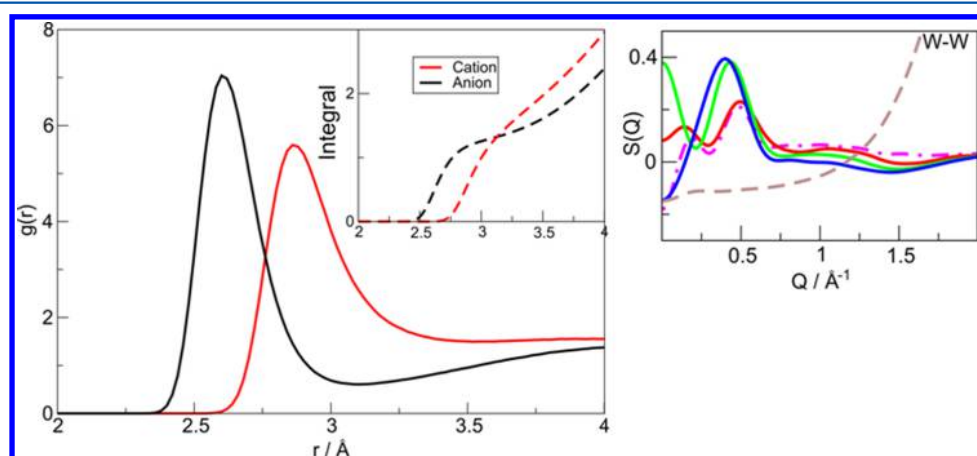

Figure 9. Left panel: ion head−water radial distribution function. Black: anion carboxylate oxygen (O1/O2)−water oxygen; Red: cation ammonium nitrogen N1−water oxygen. Peak integrals in the inset. Right panel: water−water interactions. Color codes: black χ_1, red χ_2, green χ_3, blue χ_4, magenta χ_5. In gray, the pattern for pure water (TIP4P model) is shown for comparison.

Further insights on the differences in interactions between EAB and water or NMP can be found in the $g(r)$ between ions and water or NMP (Figure S3, left graph), and between the carbon atoms of butanoate ions (Figure S3, right graph). In the case of EAB/water mixtures, we found that strong hydrogen bonds are established with anions and cations (Figure S3, left graph, top), that gradually weaken and replace cation−anion interactions, ultimately leaving a residual distance correlation between apolar alkyl chains, which is responsible for the presence of the prepeak, decreased in intensity (Figure 9 right graph, top) and at longer distances (Figure 4). Contrary to water, which can form hydrogen bonds with both cations and anions, NMP lacks the hydrogen bond donor and only has an HB acceptor (the carbonyl oxygen) that can interact with the

cation only. Therefore, in NMP mixtures, the cation−anion interactions are less affected when NMP is added (a clear "second shell" is visible, Figure 4), and the apolar interactions even increase in intensity (Figure S3 right graph, bottom) in their first shell.

■ SUMMARY

This study provides experimental and theoretical evidence, through X-ray diffraction measurements (SAXS and WAXS) and classical molecular dynamics simulations (MD), respectively, regarding the effects of water and NMP addition on the structure of the ionic liquid ethylammonium butanoate. In particular, our results indicate that the establishment of hydrogen bonds between water and EAB ions upon hydration leads to the progressive disruption of the Coulombic cation−anion interactions. This chaotropic behavior of water with respect to EAB results in the weakening, moving at lower Q and ultimate disappearance of the diffraction prepeak due to the mesoscopic structural correlations between the apolar tails mediated by the cation−anion pairing. The opposite behavior was observed for NMP, where, on the contrary, the diffraction prepeak shifts at higher Q values (corresponding to smaller distances), and was ascribed to proximity increase between EAB ions when the bulky and sphere-like NMP molecules enter the ionic liquid segregated structure. Even though the ion−ion interactions are locally enhanced, the dilution of the system with a nondirectional molecule like NMP leads to a rapid ripping and disappearance of the mesoscopic order. We intend to corroborate our findings with further experimental studies.

■ ASSOCIATED CONTENT

ⓢ Supporting Information

The Supporting Information is available free of charge on the ACS Publications website at DOI: 10.1021/acs.jpcb.7b01837.

> Comparison between experimental and simulated patterns [Figure S1 (structure functions $QI(Q)M(Q)$) and Figure S2 (Diff(r))]; radial distribution functions g(r) between ions and water/NMP for the intermediate composition χ_3 [Figure S3]; pictorial view of water intercalation into the ionic liquid [Figure S4]; complete author list of ref 34 (PDF)

■ AUTHOR INFORMATION

Corresponding Author

*E-mail: lorenzo.gontrani@uniroma1.it

ORCID ⓘ

Lorenzo Gontrani: 0000-0001-8212-7029

Notes

The authors declare no competing financial interest.

■ ACKNOWLEDGMENTS

■ REFERENCES

(1) Plechkova, N. V.; Seddon, K. R. Applications of Ionic Liquids in The Chemical Industry. *Chem. Soc. Rev.* **2008**, *37*, 123−150.

(2) Osteryoung, R. A.; Gale, R. J.; Robinson, J.; Linga, H.; Cheek, G. Chemical and Electrochemical Studies in a Room-Temperature Ionic Liquid. *J. Electrochem. Soc.* **1981**, *128*, C79−C79.

(3) Canongia Lopes, J. N.; Shimizu, K.; Padua, A. A. H.; Umebayashi, Y.; Fukuda, S.; Fujii, K.; Ishiguro, S. A Tale of Two Ions: The Conformational Landscapes of Bis(trifluoromethanesulfonyl)amide and N,N-Dialkylpyrrolidinium. *J. Phys. Chem. B* **2008**, *112*, 1465−1472.

(4) Greaves, T. L.; Drummond, C. Protic Ionic Liquids: Properties and Applications. *Chem. Rev.* **2008**, *108*, 206.

(5) Yoshizawa, M.; Xu, W.; Angell, C. A. Ionic Liquids by Proton Transfer: Vapor Pressure, Conductivity, and the Relevance of ΔpKa from Aqueous Solutions. *J. Am. Chem. Soc.* **2003**, *125*, 15411.

(6) Walden, P. Über die Molekulargrösse und Elektrische Leitfähigkeit Einiger Geschmolzenen Salze. *Bull. Acad. Imper. Sci.* **1914**, *8* (2), 405−422.

(7) Hardacre, C.; Holbrey, J. D.; McMath, S. E. J.; Bowron, D. T.; Soper, A. K. Structure of Molten 1,3-Dimethylimidazolium Chloride Using Neutron Diffraction. *J. Chem. Phys.* **2003**, *118*, 273−278.

(8) Dieter, K. M.; Dymek, C. J., Jr.; Heimer, N. E.; Rovang, J. W.; Wilkes, J. S. Ionic Structure and Interactions in 1-Methyl-3-ethylimidazolium Chloride-AICl3 Molten Salts. *J. Am. Chem. Soc.* **1988**, *110*, 2722−2726.

(9) Bankmann, D.; Giernoth, R. Magnetic Resonance Spectroscopy in Ionic Liquids. *Prog. Nucl. Magn. Reson. Spectrosc.* **2007**, *51*, 63−90.

(10) Wang, J.; Wang, H. Aggregation in Systems of Ionic Liquids. In *Structure and Interactions of Ionic Liquids*; Springer-Verlag: Berlin Heidelberg, 2014; Vol. 151, pp 47−85.

(11) Campetella, M; Martino Chillura, D.; Scarpellini, E.; Gontrani, L. Low-Q peak in X-Ray Patterns of Choline-Phenylalanine and -Homophenylalanine: A Combined Effect of Chain and Stacking. *Chem. Phys. Lett.* **2016**, *660*, 99−101.

(12) Hayes, R.; Imberti, S.; Warr, G. G.; Atkin, R. Effect of Cation Alkyl Chain Length and Anion Type on Protic Ionic Liquid Nanostructure. *J. Phys. Chem. C* **2014**, *118*, 13998−14008.

(13) Greaves, T. L.; Mudie, S. T.; Drummond, C. J. Effect of Protic Ionic Liquids (PILs) on the Formation of Non-Ionic Dodecylpoly-(ethylene oxide) Surfactant Self-Assembly Structures and the Effect of These Surfactants on the Nanostructure of PILs. *Phys. Chem. Chem. Phys.* **2011**, *13*, 20441−20452.

(14) Greaves, T. L.; Kennedy, D. F.; Mudie, S. T.; Drummond, C. J. *J. Phys. Chem. B* **2010**, *114*, 10022−10031.

(15) Urahata, S. M.; Ribeiro, M. C. C. Structure of ionic liquids of 1-alkyl-3-methylimidazolium cations: A Systematic Computer Simulation Study. *J. Chem. Phys.* **2004**, *120*, 1855.

(16) Annapureddy, H. V. R.; Hu, Z.; Xia, J.; Margulis, C. J. How Does Water Affect the Dynamics of the Room-Temperature Ionic Liquid 1-Hexyl-3-methylimidazolium Hexafluorophosphate and the Fluorescence Spectroscopy of Coumarin-153 When Dissolved in It? *J. Phys. Chem. B* **2008**, *112*, 1770−1776.

(17) Reddy, P. N.; Padmaja, P.; Subba Reddy, B. V.; Rambabu, G. Ionic liquid/Water Mixtures Promoted Organic Transformations. *RSC Adv.* **2015**, *5*, 51035−51054.

(18) Shah, F. U.; Glavatskih, S.; MacFarlane, D. R.; Somers, A.; Forsyth, M.; Antzutkin, O. N. Novel Halogen-Free Chelated Orthoborate-Phosphonium Ionic Liquids: Synthesis and Tribophysical Properties. *Phys. Chem. Chem. Phys.* **2011**, *13*, 12865−12873.

(19) Cammarata, L.; Kazarian, S. G.; Salter, P. A.; Welton, T. Molecular States of Water in Room Temperature Ionic Liquids. *Phys. Chem. Chem. Phys.* **2001**, *3*, 5192−5200.

(20) Driver, G. C. Aqueous Brønsted−Lowry Chemistry of Ionic Liquid Ions. *ChemPhysChem* **2015**, *16*, 2432−2439.

(21) Usula, M.; Plechkova, N. V.; Piras, A.; Porcedda, S. Ethylammoniumalkanoate-based ionic liquid + water mixtures. *J. Therm. Anal. Calorim.* **2015**, *121*, 1129−1137.

(22) Salma, U.; Usula, M.; Caminiti, R.; Gontrani, L.; Plechkova, N. V.; Seddon, K. R. X-Ray and Molecular Dynamics Studies of Butylammonium Butanoate−Water Binary Mixtures. *Phys. Chem. Chem. Phys.* **2017**, *19*, 1975−1981.

(23) Salma, U.; Ballirano, P.; Usula, M.; Caminiti, R.; Plechkova, N. V.; Seddon, K. R.; Gontrani, L. A New Insight Into the Nanostructure of Alkylammoniumalkanoates Based Ionic Liquids in Water. *Phys. Chem. Chem. Phys.* **2016**, *18*, 11497−11502.

(24) Usula, M.; Plechkova, N. V.; Piras, A.; Porcedda, S. Ethylammoniumalkanoate-Based Ionic Liquid + Water Mixtures. *J. Therm. Anal. Calorim.* **2015**, *121*, 1129−1137.

(25) Caminiti, R.; Carbone, M.; Mancini, G.; Sadun, C. Study of Cetyltrialkylammonium Bromide and Tribromide Salts in the Solid Phase. *J. Mater. Chem.* **1997**, *7*, 1331−1337.

(26) Keen, D. A. A Comparison of Various Commonly Used Correlation Functions for Describing Total Scattering. *J. Appl. Crystallogr.* **2001**, *34*, 172−177.

(27) Gontrani, L.; Ramondo, F.; Caracciolo, G.; Caminiti, R. A Study of Cyclohexane, Piperidine and Morpholine with X-Ray Diffraction and Molecular Simulations. *J. Mol. Liq.* **2008**, *139*, 23−28.

(28) Gontrani, L.; Ramondo, F.; Caminiti, R. Energy Dispersive X-Ray Diffraction and Molecular Dynamics Meet: The Structure of Liquid Pyrrole. *Chem. Phys. Lett.* **2006**, *417*, 200−205.

(29) Campetella, M.; Gontrani, L.; Bodo, E.; Ceccacci, F.; Marincola, F.; Caminiti, R. Conformational Isomerisms and Nano-Aggregation in Substituted Alkylammonium Nitrates Ionic Liquids: An X-Ray and Computational Study of 2-Methoxyethylammonium Nitrate. *J. Chem. Phys.* **2013**, *138* (18), 184506.

(30) Gontrani, L.; Ballirano, P.; Leonelli, F.; Caminiti, R. *The Structure of Ionic Liquids*; Caminiti, R., Gontrani, L., Eds.; Springer International Publishing: Cham, Switzerland, 2014; pp 1−37

(31) Mariani, A.; Dattani, R.; Caminiti, R.; Gontrani, L. Nanoscale Density Fluctuations in Ionic Liquid Binary Mixtures with Non-amphiphilic Compounds: First Experimental Evidence. *J. Phys. Chem. B* **2016**, *120* (40), 10540−10546.

(32) Usula, M.; Mocci, F.; Marincola, F. C.; Porcedda, S.; Gontrani, L.; Caminiti, R. The Structural Organization of N-methyl-2-Pyrrolidone+ Water Mixtures: A Densitometry, X-Ray Diffraction, and Molecular Dynamics Study. *J. Chem. Phys.* **2014**, *140*, 124503.

(33) Wang, J.; Wolf, R. M.; Caldwell, J. W.; Kollman, P. A.; Case, D. A. Development and Testing of a General Amber Force Field. *J. Comput. Chem.* **2004**, *25*, 1157.

(34) Case, D.; Darden, T.; Cheatham, T., III; Simmerling, C.; Wang, J.; Duke, R.; Luo, R.; Walker, R.; Zhang, W.; Merz, K. et al. *AMBER 12*; University of California: San Francisco, 2012.

(35) Cieplak, P.; Cornell, W. D.; Bayly, C. I.; Kollman, P. A. Application of the Multimolecule and Multiconformational RESP Methodology to Biopolymers: Charge Derivation for DNA, RNA, and Proteins. *J. Comput. Chem.* **1995**, *16*, 1357.

(36) Martinez, L.; Andrade, R.; Birgin, E. G.; Martinez, J. M. PACKMOL: A Package for Building Initial Configurations for Molecular Dynamics Simulations. *J. Comput. Chem.* **2009**, *30*, 2157.

(37) Berendsen, H. J. C.; Postma, J. P. M.; van Gunsteren, W. F.; Di Nola, A.; Haak, J. R. Molecular Dynamics with Coupling to an External Bath. *J. Chem. Phys.* **1984**, *81*, 3684−3690.

(38) *GROMACS 3.0*: a package for molecular simulation and trajectory analysis, Lindahl, E.; Hess, B.; van der Spoel, D. *J Mol Model* (2001) *7*, 306−317.

(39) Araque, J. C.; Hettige, J. J.; Margulis, C. J. Modern Room Temperature Ionic Liquids, a Simple Guide to Understanding Their Structure and How It May Relate to Dynamics. *J. Phys. Chem. B* **2015**, *119* (40), 12727−12740.

(40) Egami, T. In *From Semiconductors to Proteins: Beyond the Average Structure*; Billinge, S., Thorpe, M. F., Eds.; Springer Science & Business Media: Berlin, 2012.

(41) Gontrani, L.; Ballirano, P.; Leonelli, F.; Caminiti, R. X-ray Diffraction Studies of Ionic Liquids: From Spectra to Structure and Back. In *The Structure of Ionic Liquids*; Caminiti, R., Gontrani, L., Eds.; Springer International Publishing: Cham, Switzerland, 2014.

(42) Kashyap, H. K.; Hettige, J. J.; Annapureddy, H. V. R.; Margulis, C. J. SAXS Anti-Peaks Reveal the Length-Scales of Dual Positive−Negative and Polar−Apolar Ordering in Room-Temperature Ionic Liquids. *Chem. Commun.* **2012**, *48*, 5103−5105.

(43) Dhungana, K. B.; Faria, L. F. O.; Wu, B.; Liang, M.; Ribeiro, M. C. C.; Margulis, C. J.; Castner, E. W., Jr Structure of Ionic Liquids with Cationic Silicon-Substitutions. *J. Chem. Phys.* **2016**, *145*, 024503.